PROCEEDINGS OF SCIENCE

Octet baryon charges with $N_f = 2 + 1$ non-perturbatively improved Wilson fermions

Gunnar S. Bali,[a] **Sara Collins,**[a] **Wolfgang Söldner**[a] **and Simon Weishäupl**[a,*]

[a] *Institut für Theoretische Physik, Universität Regensburg, 93040 Regensburg, Germany.*

E-mail: gunnar.bali@ur.de, sara.collins@ur.de, wolfgang.soeldner@ur.de, simon.weishaeupl@ur.de

The axial charge of the nucleon, g_A, has been computed extensively on the lattice. However, the axial charges for other octet baryons (hyperons) such as the Σ and Ξ baryons are less well known experimentally and theoretically. Here we present the current status of our analysis for the isovector axial, scalar and tensor charges, as well as for the second Mellin moments of isovector PDFs. The scalar charges are related to the difference between the physical up and down quark masses via the vector Ward identity which allows us to determine this splitting from our result of the scalar charge of the Σ baryon. Moreover, we compute the QCD contributions to baryon isospin mass splittings. Our calculations are performed on a large set of $N_f = 2 + 1$ CLS ensembles of non-perturbatively $O(a)$ improved Wilson fermions with tree-level Symanzik improved gauge action.

European network for Particle physics, Lattice field theory and Extreme computing (EuroPLEx2023)
11-15 September 2023
Berlin, Germany

*Speaker

PoS(EuroPLEx2023)040

1. Introduction

A charge of a hadron parameterizes the strength of its interaction at small momentum transfer with a particle that couples to this particular charge. For instance, the isovector axial charge determines the β decay rate of the neutron. At the same time, this charge corresponds to the difference between the contribution of the spin of the up quarks minus the spin of the down quarks to the total longitudinal spin of a nucleon in the light front frame that is used in the collinear description of deep inelastic scattering. This intimate connection to spin physics at large virtualities and, more specifically, to the decomposition of the longitudinal proton spin into contributions of the gluon total angular momentum and the spins and angular momenta for the different quark flavours [1, 2] opens up a whole area of intense experimental and theoretical research: the first Mellin moment of the helicity structure functions $g_1(x)$ is related to the sum of the individual spins of the quarks within the proton. For lattice determinations of the individual quark contributions to its first and third moments, see, e.g., Refs. [3–7] and Ref. [8], respectively. Due to the lack of experimental data on $g_1(x)$, in particular at small Bjorken-x, and difficulties in the flavour separation, usually additional information is used in determinations of the helicity parton distribution functions (PDFs) from global fits to experimental data [9–13]. In addition to the axial charge g_A of the proton, this includes information from hyperon decays, in combination with SU(3) flavour symmetry relations whose validity need to be checked.

2. Octet baryon charges

All light baryons (i.e., baryons without charm or bottom quarks) with strangeness $S < 0$, i.e., with a net difference between the numbers of strange (s) antiquarks and quarks are usually called hyperons. The spin-1/2 baryon octet, depicted in Fig. 1, contains the nucleons $N \in \{p, n\}$, besides the $S = -1$ hyperons Λ^0 and $\Sigma \in \{\Sigma^+, \Sigma^0, \Sigma^-\}$ and the $S = -2$ hyperons $\Xi \in \{\Xi^0, \Xi^-\}$ (cascades). We assume isospin symmetry $m_\ell = m_u = m_d$, where m_ℓ corresponds to the average mass of the physical up (u) and down (d) quarks. In this case, the baryon masses within isomultiplets are degenerate.

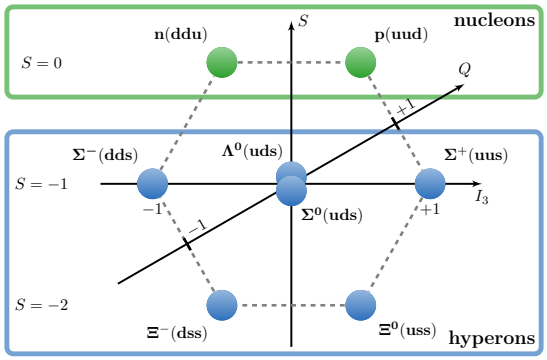

Figure 1: The spin-1/2 baryon octet where S, I_3 and $Q = (1+S)/2 + I_3$ label strangeness, isospin and charge, respectively.

The (generalized) baryon charges $g^{B'B}_{J[\mathcal{D}]}$ are obtained from matrix elements of the form

$$\langle B'(p',s')|\bar{u}\Gamma_{J[\mathcal{D}]}d|B(p,s)\rangle = g^{B'B}_{J[\mathcal{D}]}\bar{u}_{B'}(p',s')\Gamma_{J[\mathcal{D}]}u_B(p,s) \tag{1}$$

at zero four-momentum transfer $q^2 = (p'-p)^2 = 0$. Above, $u_B(p,s)$ denotes the Dirac spinor of a baryon B with four momentum p and spin s. We restrict ourselves to $\Delta I_3 = 1$ transitions within the baryon octet. In this case $p' = p$, since in isosymmetric QCD $m_{B'} = m_B$, and it is sufficient to set $\mathbf{p} = \mathbf{0}$. Rather than using the above $I_3 = 1$ currents $\bar{u}\Gamma_{J[\mathcal{D}]}d$ (where the vector and axial currents couple to the W^- boson), it is convenient to define $I_3 = 0$ isovector currents,

$$O_{J[\mathcal{D}]}(x) = \bar{u}(x)\Gamma_{J[\mathcal{D}]}u(x) - \bar{d}(x)\Gamma_{J[\mathcal{D}]}d(x), \tag{2}$$

and the corresponding (generalized) charges $g^{B}_{J[\mathcal{D}]}$,

$$\langle B(p,s)|O_{J[\mathcal{D}]}|B(p,s)\rangle = g^{B}_{J[\mathcal{D}]}\bar{u}_B(p,s)\Gamma_J u_B(p,s). \tag{3}$$

Note that we do not include the Λ baryon here since in this case the isovector combination trivially gives zero. We consider vector (V), axialvector (A), scalar (S) and tensor (T) operators which are defined through the Dirac matrices $\Gamma_J = \gamma_4, \gamma_i\gamma_5, \mathbb{1}, \sigma_{ij}$ for $J \in \{V, A, S, T\}$, with $\sigma_{\mu\nu} = \frac{1}{2}[\gamma_\mu, \gamma_\nu]$, where $i, j \in \{1,2,3\}$, $i < j$ and which give rise to the baryon isovector charges g^B_J.

In addition we analyze the twist-2 operators for $J \in \{V\mathcal{D}, A\mathcal{D}, T\mathcal{D}\}$ which include a covariant derivative $\overleftrightarrow{\mathcal{D}}_\mu = \frac{1}{2}(\overrightarrow{\mathcal{D}}_\mu - \overleftarrow{\mathcal{D}}_\mu)$ and are defined through

$$\Gamma_{V\mathcal{D}} = \gamma_4\overleftrightarrow{\mathcal{D}}_4 - \frac{1}{3}\gamma_i\overleftrightarrow{\mathcal{D}}_i, \qquad \Gamma_{A\mathcal{D}} = \gamma_{\{i}\gamma_5\overleftrightarrow{\mathcal{D}}_{4\}}, \qquad \Gamma_{T\mathcal{D}} = \sigma_{[i\{j]}\overleftrightarrow{\mathcal{D}}_{4\}}, \tag{4}$$

where $_{[i,j]}$ and $_{\{i,j\}}$ indicates anti-/ symmetrization of the indices.

The matrix elements of the twist-2 operators are related to the isovector average quark momentum fraction ($\langle x\rangle_{u-d}$) and the second isovector helicity ($\langle x\rangle_{\Delta u-\Delta d}$) and transversity ($\langle x\rangle_{\delta u-\delta d}$) moments as follows:

$$\langle B|O_{V\mathcal{D}}|B\rangle = -m_B\langle x\rangle^B_{u-d}, \quad \langle B|O_{A\mathcal{D}}|B\rangle = -\frac{im_B}{2}\langle x\rangle^B_{\Delta u-\Delta d}, \quad \langle B|O_{T\mathcal{D}}|B\rangle = -\frac{im_B}{2}\langle x\rangle^B_{\delta u-\delta d}. \tag{5}$$

3. Gauge ensembles

We employ ensembles generated with $N_f = 2+1$ flavours of non-perturbatively $O(a)$ improved Wilson fermions and a tree-level Symanzik improved gauge action, which were mostly produced within the Coordinated Lattice Simulations (CLS) [14] effort. In total 47 ensembles were analysed spanning six lattice spacings a in the range $0.039\,\text{fm} \lesssim a \lesssim 0.098\,\text{fm}$, with pion masses between 430 MeV and 130 MeV (below the physical pion mass), as shown in Fig. 2. The lattice spatial extent L is kept sufficiently large, where $LM_\pi \geq 4$ for the majority of the ensembles. A limited number of smaller volumes are employed to enable finite volume effects to be investigated, with the spatial extent varying across all the ensembles in the range $3.0 \leq LM_\pi \leq 6.5$. Further details are given in Table I of Ref. [15]. The ensembles lie along three trajectories in the quark mass plane:

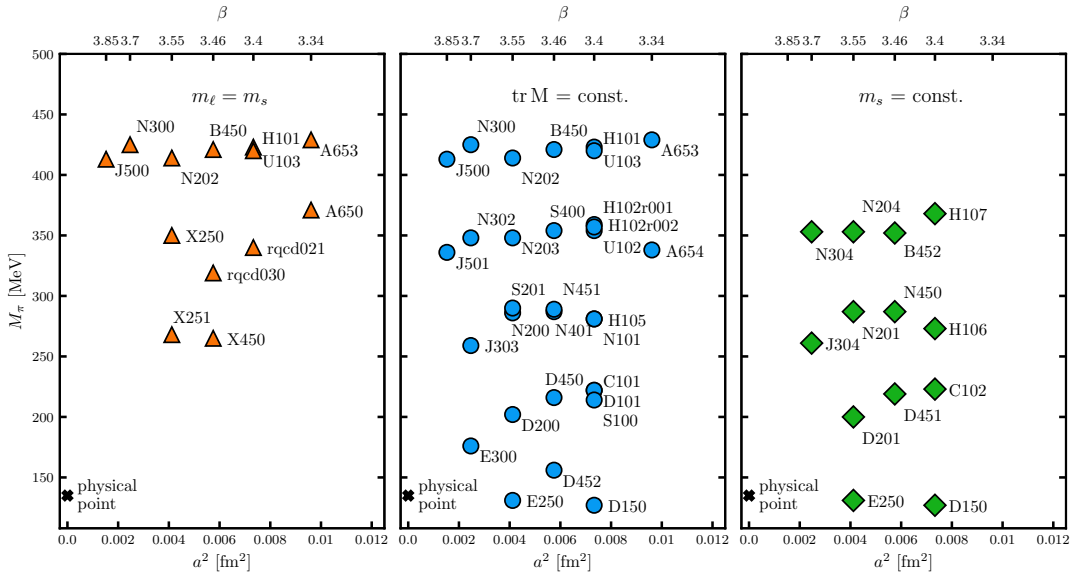

Figure 2: Parameter landscape of the analysed ensembles (listed in Table I of Ref. [15]). The ensembles are grouped according to the three quark mass trajectories (see the text): (left) the symmetric line ($m_\ell = m_s$), (middle) the tr M = const. line and (right) the m_s = const. line.

- the symmetric line: the light and strange quark masses are degenerate ($m_\ell = m_s$) and SU(3) flavour symmetry is exact.
- The tr M = const. line: starting at the $m_\ell = m_s$ flavour symmetric point, the trajectory approaches the physical point holding the trace of the quark mass matrix ($2m_\ell + m_s$, i.e., the flavour averaged quark mass) constant such that $2M_K^2 + M_\pi^2$ is close to its physical value.
- The m_s = const. line: the renormalized strange quark mass is kept near to its physical value [16].

The latter two trajectories intersect close to the physical point, whereas the symmetric line approaches the SU(3) chiral limit. The excellent coverage of the quark mass plane enables the interpolation/extrapolation of the results for the charges to the physical point to be tightly constrained. In addition, considering the wide range of lattice spacings and spatial volumes and the high statistics available for most ensembles, all sources of systematic uncertainty associated with simulating at unphysical quark mass, finite lattice spacing and finite volume can be investigated.

4. Correlation functions

The baryon octet charges are extracted from two- and three-point correlation functions of the form

$$C^B_{\text{2pt}}(t) = \mathcal{P}^{\alpha\beta}_+ \sum_{\mathbf{x}'} \langle \mathcal{B}_\alpha(\mathbf{x}', t)\ \bar{\mathcal{B}}_\beta(\mathbf{0}, 0)\rangle, \tag{6}$$

$$C^B_{\text{3pt}}(t, \tau) = \mathcal{P}^{\alpha\beta} \sum_{\mathbf{x}', \mathbf{y}} \langle \mathcal{B}_\alpha(\mathbf{x}', t) \mathcal{O}_J(\mathbf{y}, \tau) \bar{\mathcal{B}}_\beta(\mathbf{0}, 0)\rangle. \tag{7}$$

Spin-1/2 baryon states are created (annihilated) using suitable interpolators $\overline{\mathcal{B}}$ ($\mathcal{B}$): for the nucleon, Σ and Ξ, we employ interpolators corresponding to the proton, Σ^+ and Ξ^0, respectively,

$$N_\alpha = \epsilon^{ijk} u^i_\alpha \left(u^{jT} C\gamma_5 d^k\right), \quad \Sigma_\alpha = \epsilon^{ijk} u^i_\alpha \left(s^{jT} C\gamma_5 u^k\right), \quad \Xi_\alpha = \epsilon^{ijk} s^i_\alpha \left(s^{jT} C\gamma_5 u^k\right), \tag{8}$$

with spin index α, colour indices i, j, k and C being the charge conjugation matrix.

We ensure positive parity via the projection operator $\mathcal{P}_+ = \frac{1}{2}(\mathbb{1} + \gamma_4)$. For the three-point functions, $\mathcal{P} = \mathcal{P}_+$ for $J = V[\mathcal{D}], S$ and $\mathcal{P} = i\gamma_i\gamma_5\mathcal{P}_+$ for $J = A[\mathcal{D}], T[\mathcal{D}]$. The latter corresponds to taking the difference of the polarizations (in the i direction). The interpolators are constructed from spatially extended quark fields in order to increase the overlap with the ground state of interest and minimize contributions to the correlation functions from excited states. Wuppertal smearing is employed [17], together with APE-smeared [18] gauge transporters.

Performing the Wick contractions for the two- and three-point correlation functions leads to the connected quark-line diagrams. Note that there are no disconnected quark-line diagrams for the three-point functions as these cancel when forming the isovector flavour combination of the current. The two-point functions are constructed in the standard way using point-to-all propagators. For the three-point functions either a stochastic approach (described in section III C of Ref. [15]) or the sequential source method [19] (on some ensembles in combination with the coherent sink technique [20]) is employed. The stochastic approach provides a computationally cost efficient way of evaluating the three-point functions for the whole of the baryon octet, however, additional noise is introduced. The relevant measurements for the nucleon (which has the worst signal-to-noise ratio of the octet) have already been performed with the sequential source method and we use these data in our analysis and the stochastic approach for the correlation functions of the Σ and the Ξ baryons. Note that along the symmetric line ($m_\ell = m_s$) the hyperon three-point functions can be obtained as linear combinations of the contractions carried out for the currents $\bar{u}\Gamma_J u$ and $\bar{d}\Gamma_J d$ within the proton. Therefore, no stochastic three-point functions are generated in these cases.

We typically realize four source-sink separations with $t/\mathrm{fm} \approx \{0.7, 0.8, 1.0, 1.2\}$ in order to investigate excited state contamination and reliably extract the ground state baryon octet charges. Details of our fitting analysis are presented in the next section. Multiple measurements are performed per configuration, in particular for the larger source-sink separations to improve the signal, see Table I of Ref. [15].

5. Fitting and excited state analysis

The spectral decompositions of the two- and three-point correlation functions read

$$C^B_{\mathrm{2pt}}(t) = \sum_n |Z^B_n|^2 e^{-E^B_n t}\,, \tag{9}$$

$$C^B_{\mathrm{3pt}}(t,\tau;O_{J[\mathcal{D}]}) = \sum_{n,m} Z^B_n Z^{B*}_m \langle n|O_{J[\mathcal{D}]}|m\rangle e^{-E^B_n(t-\tau)} e^{E^B_m \tau}, \tag{10}$$

where E^B_n is the energy of state $|n\rangle$ ($n = 0, 1, \ldots$), created when applying the baryon interpolator $\bar{\mathcal{B}}$ to the vacuum state $|\Omega\rangle$ and Z^B_n is the associated overlap factor $Z^B_n \propto \langle n|\bar{\mathcal{B}}|\Omega\rangle$. The ground state matrix elements of interest $\langle 0|O_{J[\mathcal{D}]}|0\rangle = g^{B,\mathrm{latt}}_{J[\mathcal{D}]}$ can be obtained in the limit of large time

separations from the ratio of the three-point and two-point functions

$$R^B_{J[\mathcal{D}]}(t,\tau) = \frac{C^B_{\text{3pt}}(t,\tau;O_{J[\mathcal{D}]})}{C^B_{\text{2pt}}(t)} \overset{t,\tau\to\infty}{\longrightarrow} g^{B,\text{latt}}_{J[\mathcal{D}]}. \tag{11}$$

However, the signal-to-noise ratio of the correlation functions deteriorates exponentially with the time separation and with current techniques it is not possible to achieve a reasonable signal for separations that are large enough to ensure ground state dominance. At moderate t and τ, one observes significant excited state contributions to the ratio.

In Ref. [15] we extract the charges by fitting to the ratio of correlation functions using a fit form which takes into account contributions from up to two excited states,

$$\begin{aligned} R^B_J(t,\tau) = b^J_0 &+ b^J_1\left(e^{-\Delta E_1(t-\tau)} + e^{-\Delta E_1\tau}\right) + b^J_2 e^{-\Delta E_1 t} \\ &+ b^J_3\left(e^{-\Delta E_2(t-\tau)} + e^{-\Delta E_2\tau}\right) + b^J_4 e^{-\Delta E_2 t}, \end{aligned} \tag{12}$$

where $\Delta E_n = E^B_n - E^B_0$ denotes the energy gap between the ground state and the n^{th} excited state of baryon B and we have not included transitions between the first and the second excited state. The amplitude $b^J_0 = g^{B,\text{latt}}_J$ gives the charge, while $b^J_{1,3}$ and $b^J_{2,4}$ are related to the ground state to excited state and excited state to excited state transition matrix elements, respectively. In practice, even when simultaneously fitting to all available source-sink separations, it is difficult to determine the energy gaps (and amplitudes) for a particular channel J. Similar to the strategy pursued in

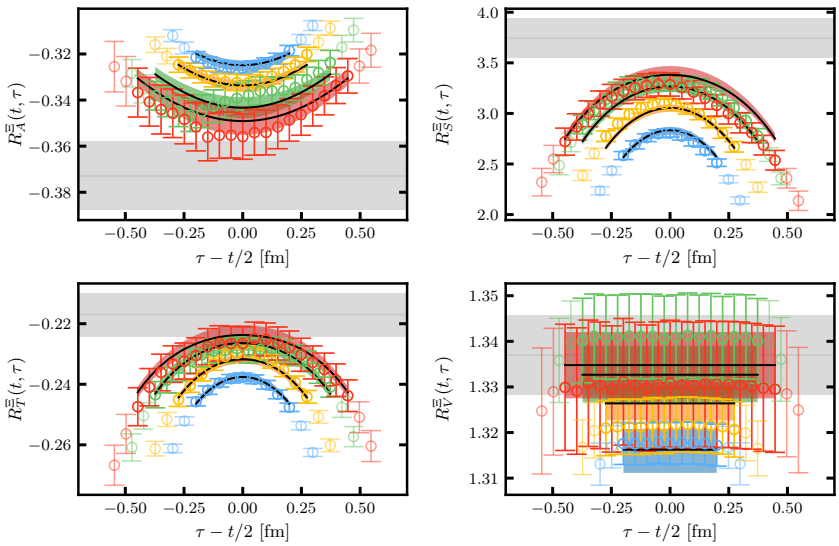

Figure 3: Unrenormalized ratios $R^\Xi_J(t,\tau)$, $J \in \{A,S,T,V\}$ (defined in Eq. (11)) for the cascade baryon on ensemble N302 ($M_\pi = 348\,\text{MeV}$ and $a = 0.049\,\text{fm}$), where $t \approx \{0.7, 0.8, 1.0, 1.2\}\,\text{fm}$. The grey horizontal lines and bands show the results for the ground state matrix elements $\langle 0|\bar{u}\Gamma_J u - \bar{d}\Gamma_J d|0\rangle = g^{\Xi,\text{latt}}_J$, obtained from a simultaneous fit to the ratios for all channels and source-sink separations using parametrization 7 (see Eq. (12) and Table II of Ref. [15]). The data points with $\tau \in [\delta t, t - \delta t]$, where $\delta t = 2a$, are included in the fit (the faded data points are omitted), which is the maximum fit range possible for our action. The coloured curves show the expectation from the fit for each source-sink separation.

Ref. [21], we simultaneously fit to all four channels $J \in \{V, A, S, T\}$ for a given baryon. In order to extract the second Mellin moments we also include the channels with $J \in \{V\mathcal{D}, A\mathcal{D}, T\mathcal{D}\}$ in the simultaneous fits. As the same energy gaps are present, the overall number of fit parameters is reduced and the fits are further constrained. A typical fit to the ratios for the cascade baryon is shown in Fig. 3.

To ensure that the excited state contributions are sufficiently under control, we carry out a variety of different fits, were we vary the data sets included in the fit, the parametrization (including either one or two excited states) and the fit range. For further details we refer to Sec. III. D of Ref. [15].

6. Chiral and continuum extrapolation of the baryon charges

The renormalized[1] charges g_J^B determined at unphysical quark masses and finite lattice spacing and spatial volume are extrapolated to the physical point in the continuum and infinite volume limits. We employ a similar strategy to the one outlined in Ref. [22] and choose continuum fit functions of the form

$$g_J^B(M_\pi, M_K, L, a = 0) = c_0 + c_\pi M_\pi^2 + c_K M_K^2 + c_V M_\pi^2 \frac{e^{-LM_\pi}}{\sqrt{LM_\pi}}, \tag{13}$$

to parameterize the quark mass and finite volume dependence, where L is the spatial lattice extent and the coefficients $c_X, X \in \{0, \pi, K, V\}$ are understood to depend on the baryon B and the current J. The leading order coefficients c_0 give the charges in the SU(3) chiral limit, which can be expressed in terms of two LECs, e.g., F and D, for the axial charges. Lattice spacing effects also need to be taken into account and we add both mass independent and mass dependent terms to the continuum fit ansatz to give

$$g_J^B(M_\pi, M_K, L, a) = g_J^B(\mathcal{M}_\pi, \mathcal{M}_K, L, 0) + c_a\, \mathbb{a}^2 + \bar{c}_a \overline{\mathcal{M}}^2\, \mathbb{a}^2 + \delta c_a \delta\mathcal{M}^2\, \mathbb{a}^2, \tag{14}$$

where $\overline{\mathcal{M}}^2 = (2\mathcal{M}_K^2 + \mathcal{M}_\pi^2)/3$ and $\delta\mathcal{M}^2 = \mathcal{M}_K^2 - \mathcal{M}_\pi^2$. The meson masses are rescaled with the Wilson flow scale t_0 [23], $\mathcal{M}_{\pi,K} = \sqrt{8t_0} M_{\pi,K}$ to form dimensionless combinations and we translate between different lattice spacings using $t_0^\star$, the value of t_0 along the symmetric line where $12t_0^* M_\pi^2 = 1.110$ [24], i.e., $\mathbb{a} = a/\sqrt{8t_0^\star}$. For more details on the scaling parameters used in the analysis, see Sec. III. F of Ref. [15]. The systematic uncertainty in the determination of the charges at the physical point is investigated by varying the fit model and by employing different cuts on the ensembles that enter the fits. Our final results are obtained by carrying out the averaging procedure described in Appendix B of Ref. [22] which gives an average and error that incorporates both the statistical and systematic uncertainties. Fig. 4 illustrates the simultaneous quark mass, continuum and finite volume extrapolations of the isovector nucleon tensor charge g_T^N and the axial charge of the cascade baryon g_A^Ξ.

[1]The isovector lattice charges, $g_J^{B,\text{latt}}$ need to be matched to the continuum $\overline{\text{MS}}$ scheme. For details on the non-perturbative renormalization and improvement see Ref. [15], in particular Sec. III D, where we also investigate the systematic uncertainties associated with the different determinations of the renormalization factors.

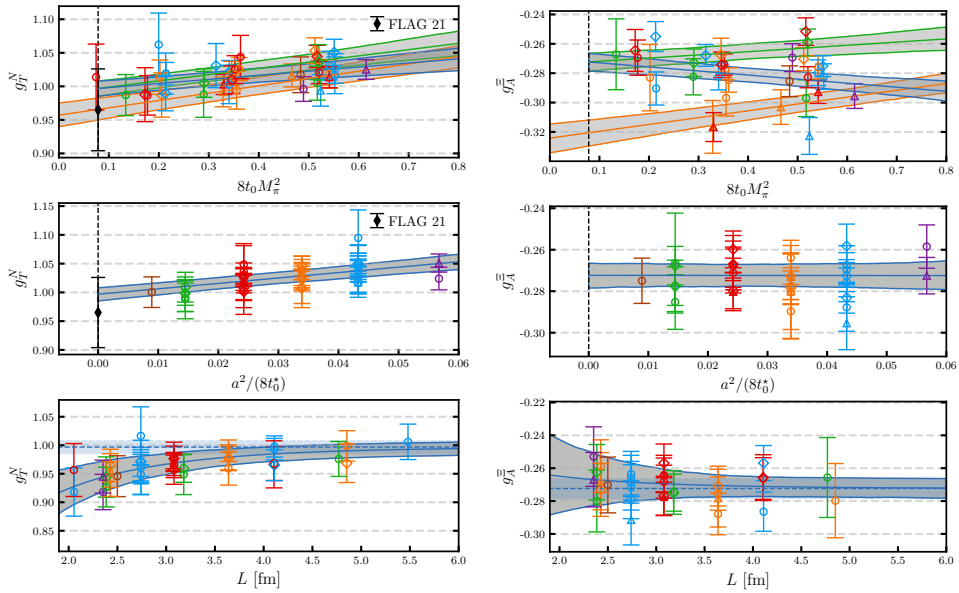

Figure 4: Simultaneous quark mass, continuum and finite volume extrapolations of g_T^N (left) and g_A^Ξ (right), extracted on ensembles with $M_\pi < 400\,\text{MeV}$. (Top) Pion mass dependence where the data points are corrected, using the fit, for finite volume and discretization effects and shifted (depending on the ensemble) to kaon masses corresponding to the tr M = const. and m_s = const. trajectories. The fit is shown as a grey band with the three trajectories distinguished by blue (tr M = const., circles), green (m_s = const., diamonds) and orange ($m_s = m_\ell$, triangles) lines, respectively. The vertical dashed line indicates the physical point. (Middle) Lattice spacing dependence at the physical point in the infinite volume limit. (Bottom) Finite volume dependence at the physical point in the continuum limit. The dashed blue line (band) indicates the infinite volume result.

7. Results of the octet baryon charges

Our final results for the axial, scalar and tensor charges [15] read

$$g_A^N = 1.284^{(28)}_{(27)}, \qquad g_A^\Sigma = 0.875^{(30)}_{(39)}, \qquad g_A^\Xi = -0.267^{(13)}_{(12)}, \tag{15}$$

$$g_S^N = 1.11^{(14)}_{(16)}, \qquad g_S^\Sigma = 3.98^{(22)}_{(24)}, \qquad g_S^\Xi = 2.57^{(11)}_{(11)}, \tag{16}$$

$$g_T^N = 0.984^{(19)}_{(29)}, \qquad g_T^\Sigma = 0.798^{(15)}_{(21)}, \qquad g_T^\Xi = -0.1872^{(59)}_{(41)}. \tag{17}$$

The result for the nucleon axial charge compares favourably with the experimental value $g_A^N/g_V^N = 1.2754(13)$ [25] and the FLAG 21 [26] average for $N_f = 2+1$, $g_A^N = 1.248(23)$ [21, 27]. A compilation of results for g_A^N is displayed in Fig. 5, which also shows lattice and phenomenological determinations of the hyperon axial charges. Within errors, the lattice results for the hyperons are consistent apart from the rather low value for g_A^Σ from ETMC [28] and the rather high value for g_A^Ξ from QCDSF-UKQCD-CSSM [29]. The phenomenological estimates for g_A^Σ are in reasonable agreement with our value, while there is a large spread in the expectations for g_A^Ξ. For the nucleon scalar and tensor charges (at $\mu = 2\,\text{GeV}$) both result agree with the FLAG 21 [26] values $g_S^N = 1.13(14)$ [21], $g_T^N = 0.965(61)$ [21] for $N_f = 2+1$ and other recent lattice studies, see

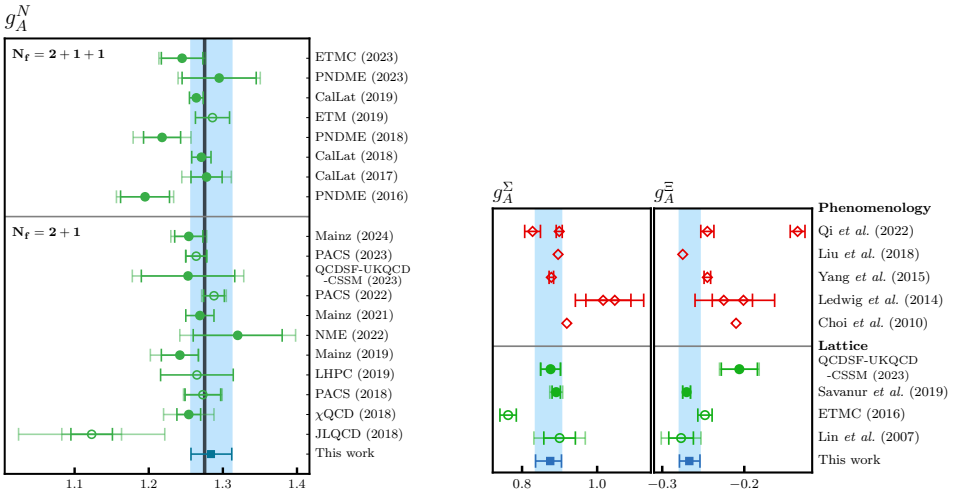

Figure 5: Right: Compilation of recent lattice determinations of the nucleon axial charge g_A^N. The vertical black line gives the experimental result [25]. Left: Comparison of our results for the axial charges g_A^Σ and g_A^Ξ (blue symbols and error bands) with other lattice determinations and phenomenological estimates. Values with filled symbols were obtained via a chiral, continuum and finite volume extrapolation. All results are converted to our phase and normalization conventions. In comparison to Fig. 25 of Ref. [15], this figure includes additional data points from PACS (2023) [30], Mainz (2024) [31] and ETMC (2023) [32]. For the other corresponding references, see Ref. [15].

Fig. 6. There is only one previous lattice determination of the hyperon scalar and tensor couplings by QCDSF-UKQCD-CSSM [29].

Our results on the scalar charges, in particular, g_S^Σ, enable us to determine the quark mass splitting $\delta_m = m_u - m_d$. The vector Ward identity relates δ_m to the QCD contributions to baryon mass splittings within an isomultiplet. In particular, to leading order in $\delta_m/\Lambda_{\mathrm{QCD}}$ and α_{QED}, the difference between the Σ^+ and Σ^- baryon masses is a pure QCD effect and one finds $\Delta m_\Sigma^{\mathrm{QCD}} = (m_{\Sigma^+} - m_{\Sigma^-})/2 = -4.04(4)$ MeV. The Lorentz decomposition of the on-shell QCD matrix element for the isovector vector current between baryons $B' = B^{Q+1}$ and $B = B^Q$ (that differ by $\Delta I_3 = 1$ in their isospin) gives (see Eq. (1))

$$i\partial^\mu \langle B'(p')|\bar{d}\gamma_\mu u|B(p)\rangle = g_V^{B'B} i\partial^\mu \bar{u}_{B'}(p')\gamma_\mu u_B(p) = g_V^{B'B}\Delta m_B^{\mathrm{QCD}}[1 + O(\delta_m/\Lambda_{\mathrm{QCD}})], \quad (18)$$

where the leading correction is due to $q_0 = p_0' - p_0 = \Delta m_B^{\mathrm{QCD}} = |\mathbf{q}|$. Combining this with the vector Ward identity $i\partial^\mu \bar{d}\gamma_\mu u = (m_u - m_d)\bar{d}u$ one finds

$$\delta_m = m_u - m_d = \frac{g_V^B}{g_S^B}\Delta m_B^{\mathrm{QCD}}, \quad (19)$$

which we refer to as the CVC relation. Using our physical point, continuum and infinite volume limit result $g_S^\Sigma = 3.98^{(22)}_{(24)}$, assuming $g_V^\Sigma = 2$ and applying Eq. (19) for the Σ baryon, we obtain in the $N_f = 3$ $\overline{\mathrm{MS}}$ scheme at $\mu = 2\,\mathrm{GeV}$

$$\delta_m = m_u - m_d = -2.03^{(12)}_{(12)}\,\mathrm{MeV}. \quad (20)$$

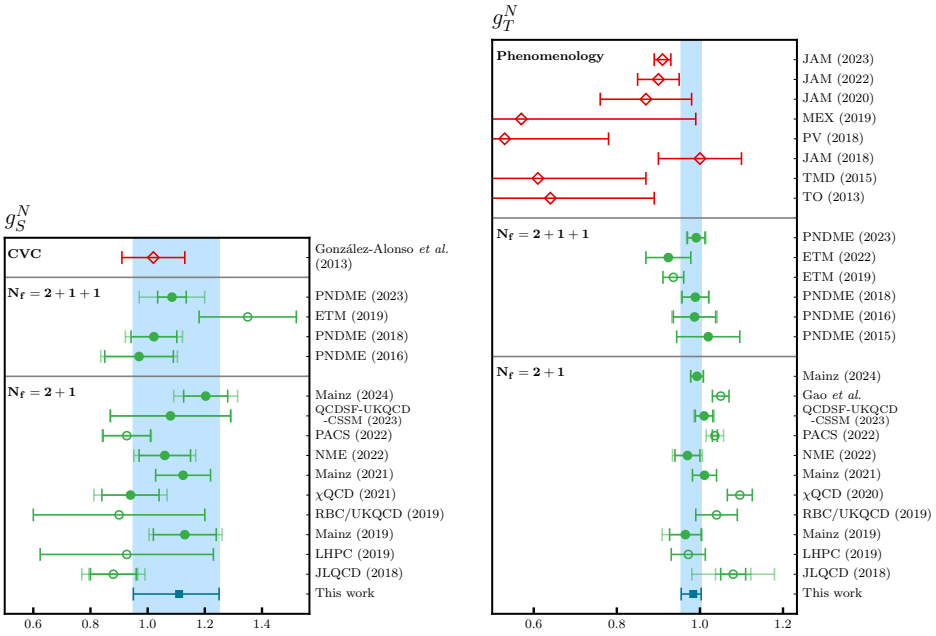

Figure 6: As in Fig. 5 for the nucleon scalar g_S^N (left) and tensor g_T^N (right) charges. González-Alonso *et al.* estimate the scalar charge via the conserved vector current (CVC) relation [33]. For the nucleon tensor charges recent phenomenological estimates are also displayed for comparison. The filled ETM (2022) [34] point is obtained from a continuum limit extrapolation of results determined on three physical point ensembles with large spatial volumes. In comparison to Figs. 28 and 29 of Ref. [15], this figure includes additional data from Mainz (2024) [31], Gao *et al.* [35] and JAM (2023) [36].

For more details and a comparison of our value with results from the literature see Sec. V. C in Ref. [15], while in Sec. V. D therein we detail our results for the QCD contributions to the isospin mass splittings $\Delta m_B^{\mathrm{QCD}}$.

8. Summary and outlook

In Ref. [15] we determined the axial, scalar and tensor isovector charges of the nucleon, sigma and cascade baryons using $N_f = 2 + 1$ lattice QCD simulations. Simultaneous extrapolations to the physical point in the continuum and infinite volume limit are performed. Systematic errors are assessed by imposing cuts on the pion mass, the lattice spacing and the volume as well as using different sets of renormalization factors. In the near future, we will update this analysis to include more ensembles and significantly increase the number of measurements on the available set of ensembles. Furthermore, we will extend the analysis to include the isovector average quark momentum fraction $\langle x \rangle^B_{u-d}$, as well as the second isovector helicity $\langle x \rangle^B_{\Delta u - \Delta d}$ and transversity $\langle x \rangle^B_{\delta u - \delta d}$ moments for the octet baryons. Preliminary results for the nucleon second moments are shown in Fig. 7. This work is a first step towards determining hyperon decay form factors which are relevant for the study of CP violation [55], while a complementary study of the baryon octet σ terms on the same data set as used here is already ongoing [56].

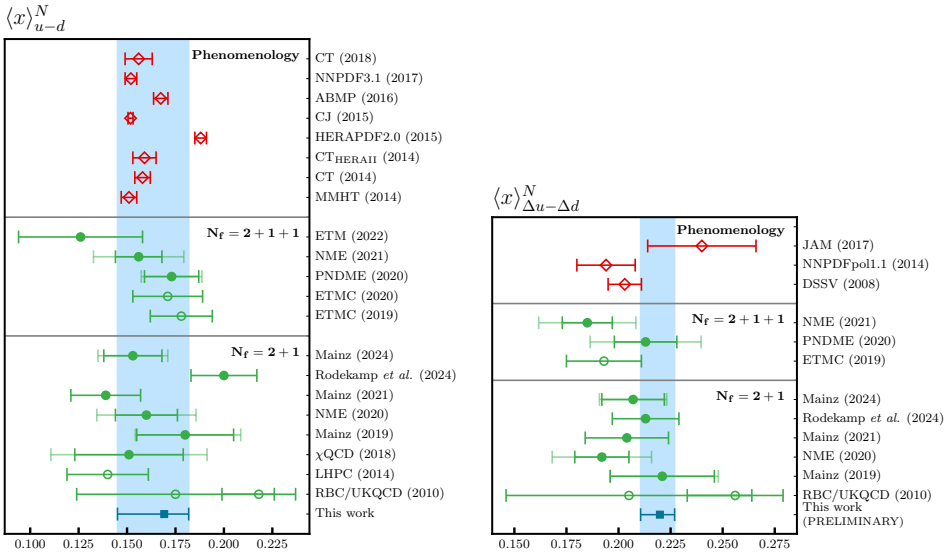

Figure 7: As in Fig. 5. Left: Isovector average quark momentum fraction $\langle x \rangle^N_{u-d}$ with $N_f = 2+1$ [21, 37–42] and $N_f = 2+1+1$ [34, 43–46] dynamical fermions. Recent phenomenological estimates are also displayed for comparison [47–53]. The filled ETM (2022) [34] point is obtained from a continuum limit extrapolation of results determined on three physical point ensembles with large spatial volumes. Right: Second isovector helicity moment $\langle x \rangle^N_{\Delta u-\Delta d}$ with $N_f = 2+1$ [21, 37, 40–42] and $N_f = 2+1+1$ [43, 45, 46] dynamical fermions. Recent phenomenological estimates are also displayed for comparison [11, 13, 54]. The Rodekamp *et al.* [42] points are obtained from a continuum limit extrapolation of results determined on two physical point ensembles.

Acknowledgments

S.C. and S.W. received support through the German Research Foundation (DFG) grant CO 758/1-1. The work of G.B. was funded in part by the German Federal Ministry of Education and Research (BMBF) grant no. 05P18WRFP1. Additional support from the European Union's Horizon 2020 research and innovation programme under the Marie Skłodowska-Curie grant agreement no. 813942 (ITN EuroPLEx) and grant agreement no. 824093 (STRONG 2020) is gratefully acknowledged, as well as initial stage funding through the German Research Foundation (DFG) collaborative research centre SFB/TRR-55.

The authors gratefully acknowledge the Gauss Centre for Supercomputing (GCS) for providing computing time through the John von Neumann Institute for Computing (NIC) on the supercomputer JUWELS [57] and in particular on the Booster partition of the supercomputer JURECA [58] at Jülich Supercomputing Centre (JSC). GCS is the alliance of the three national supercomputing centres HLRS (Universität Stuttgart), JSC (Forschungszentrum Jülich), and LRZ (Bayerische Akademie der Wissenschaften), funded by the BMBF and the German State Ministries for Research of Baden-Württemberg (MWK), Bayern (StMWFK) and Nordrhein-Westfalen (MIWF). Additional simulations were carried out on the QPACE 3 Xeon Phi cluster of SFB/TRR-55 and the Regensburg Athene 2 Cluster. The authors also thank the JSC for their support and for providing services and computing time on the HDF Cloud cluster [59] at JSC, funded via the Helmholtz Data Federation (HDF) programme.

We thank all our Coordinated Lattice Simulations (CLS) colleagues for discussions and the joint production of the gauge ensembles used. Most of the ensembles were generated using openQCD [60] within the CLS effort. A few additional ensembles were generated employing the BQCD-code [61] on the QPACE supercomputer of SFB/TRR-55. For the computation of hadronic two- and three-point functions we used a modified version of the Chroma [62] software package along with the LibHadronAnalysis library and the multigrid solver implementation of Refs. [63, 64] (see also ref. [65]) as well as the IDFLS solver [66] of openQCD. We used Matplotlib [67] to create the figures.

References

[1] X.-D. Ji, *Gauge-invariant decomposition of nucleon spin*, *Phys. Rev. Lett.* **78** (1997) 610 [hep-ph/9603249].

[2] R. L. Jaffe et al., *The g_1 problem: Fact and fantasy on the spin of the proton*, *Nucl. Phys. B* **337** (1990) 509.

[3] QCDSF collaboration, *Strangeness contribution to the proton spin from lattice QCD*, *Phys. Rev. Lett.* **108** (2012) 222001 [1112.3354].

[4] M. Engelhardt, *Strange quark contributions to nucleon mass and spin from lattice QCD*, *Phys. Rev. D* **86** (2012) 114510 [1210.0025].

[5] χQCD collaboration, *Strange and charm quark spins from the anomalous Ward identity*, *Phys. Rev. D* **95** (2017) 114509 [1511.03671].

[6] ETM collaboration, *Nucleon spin and momentum decomposition using lattice QCD simulations*, *Phys. Rev. Lett.* **119** (2017) 142002 [1706.02973].

[7] J. Green et al., *Up, down, and strange nucleon axial form factors from lattice QCD*, *Phys. Rev. D* **95** (2017) 114502 [1703.06703].

[8] RQCD collaboration, *Lattice results for the longitudinal spin structure and color forces on quarks in a nucleon*, *Phys. Rev. D* **105** (2022) 054504 [2111.08306].

[9] D. de Florian et al., *Global analysis of helicity parton densities and their uncertainties*, *Phys. Rev. Lett.* **101** (2008) 072001 [0804.0422].

[10] J. Blümlein et al., *QCD analysis of polarized deep inelastic scattering data*, *Nucl. Phys. B* **841** (2010) 205 [1005.3113].

[11] NNPDF collaboration, *A first unbiased global determination of polarized PDFs and their uncertainties*, *Nucl. Phys. B* **887** (2014) 276 [1406.5539].

[12] JAM collaboration, *Iterative Monte Carlo analysis of spin-dependent parton distributions*, *Phys. Rev. D* **93** (2016) 074005 [1601.07782].

[13] JAM collaboration, *First simultaneous extraction of spin-dependent parton distributions and fragmentation functions from a global QCD analysis*, *Phys. Rev. Lett.* **119** (2017) 132001 [1705.05889].

[14] CLS Effort collaboration, *Simulation of QCD with $N_f = 2 + 1$ flavors of non-perturbatively improved Wilson fermions*, *J. High Energy Phys.* **02** (2015) 043 [1411.3982].

[15] RQCD collaboration, *Octet baryon isovector charges from $N_f = 2 + 1$ lattice QCD*, *Phys. Rev. D* (2023) [2305.04717].

[16] RQCD collaboration, *Lattice simulations with $N_f = 2+1$ improved Wilson fermions at a fixed strange quark mass*, *Phys. Rev. D* **94** (2016) 074501 [1606.09039].
[17] S. Güsken et al., *Nonsinglet axial vector couplings of the baryon octet in lattice QCD*, *Phys. Lett. B* **227** (1989) 266.
[18] APE collaboration, *Again on SU(3) glueball mass*, *Nucl. Phys.* **B251** (1985) 624.
[19] L. Maiani et al., *Scalar densities and baryon mass differences in lattice QCD with Wilson fermions*, *Nucl. Phys.* **B293** (1987) 420.
[20] LHP collaboration, *Nucleon structure from mixed action calculations using $2+1$ flavors of asqtad sea and domain wall valence fermions*, *Phys. Rev. D* **82** (2010) 094502 [1001.3620].
[21] T. Harris et al., *Nucleon isovector charges and twist-2 matrix elements with $N_f = 2+1$ dynamical Wilson quarks*, *Phys. Rev. D* **100** (2019) 034513 [1905.01291].
[22] RQCD collaboration, *Leading order mesonic and baryonic SU(3) low energy constants from $N_f = 3$ lattice QCD*, *Phys. Rev. D* **105** (2022) 054516 [2201.05591].
[23] M. Lüscher, *Properties and uses of the Wilson flow in lattice QCD*, *J. High Energy Phys.* **08** (2010) 071 [1006.4518].
[24] M. Bruno et al., *Setting the scale for the CLS $2+1$ flavor ensembles*, *Phys. Rev. D* **95** (2017) 074504 [1608.08900].
[25] Particle Data Group collaboration, *Review of Particle Physics*, *Prog. Theor. Exp. Phys.* **2022** (2022) 083C01.
[26] Flavour Lattice Averaging Group (FLAG) collaboration, *FLAG Review 2021*, *Eur. Phys. J. C* **82** (2022) 869 [2111.09849].
[27] χQCD collaboration, *Quark spins and anomalous Ward identity*, *Phys. Rev. D* **98** (2018) 074505 [1806.08366].
[28] ETM collaboration, *Axial charges of hyperons and charmed baryons using $N_f = 2+1+1$ twisted mass fermions*, *Phys. Rev. D* **94** (2016) 034502 [1606.01650].
[29] QCDSF/UKQCD/CSSM collaboration, *Constraining beyond the standard model nucleon isovector charges*, *Phys. Rev. D* **108** (2023) 094511 [2304.02866].
[30] PACS collaboration, *Nucleon form factors in $N_f = 2+1$ lattice QCD at the physical point : finite lattice spacing effect on the root-mean-square radii*, 2311.10345.
[31] D. Djukanovic et al., *Improved analysis of isovector nucleon matrix elements with $N_f = 2+1$ flavors of $O(a)$ improved Wilson fermions*, 2402.03024.
[32] C. Alexandrou et al., *Nucleon axial and pseudoscalar form factors using twisted-mass fermion ensembles at the physical point*, 2309.05774.
[33] M. González-Alonso et al., *Isospin breaking in the nucleon mass and the sensitivity of β decays to new physics*, *Phys. Rev. Lett.* **112** (2014) 042501 [1309.4434].
[34] ETM collaboration, *Moments of the nucleon transverse quark spin densities using lattice QCD*, *Phys. Rev. D* **107** (2023) 054504 [2202.09871].
[35] X. Gao et al., *Transversity PDFs of the proton from lattice QCD with physical quark masses*, 2310.19047.
[36] C. Cocuzza et al., *First Simultaneous Global QCD Analysis of Dihadron Fragmentation Functions and Transversity Parton Distribution Functions*, 2308.14857.
[37] Y. Aoki et al., *Nucleon isovector structure functions in (2+1)-flavor QCD with domain wall fermions*, *Phys. Rev. D* **82** (2010) 014501 [1003.3387].

[38] J. R. Green et al., *Nucleon Structure from Lattice QCD Using a Nearly Physical Pion Mass*, *Phys. Lett. B* **734** (2014) 290 [1209.1687].

[39] Y.-B. Yang et al., *Proton Mass Decomposition from the QCD Energy Momentum Tensor*, *Phys. Rev. Lett.* **121** (2018) 212001 [1808.08677].

[40] Nucleon Matrix Elements (NME) collaboration, *Nucleon momentum fraction, helicity and transversity from 2+1-flavor lattice QCD*, *JHEP* **21** (2020) 004 [2011.12787].

[41] K. Ottnad et al., *Improved analysis of nucleon isovector charges and twist-2 matrix elements on CLS $N_f = 2 + 1$ ensembles*, *Proc. Sci.* **LATTICE2021** (2022) 343 [2110.10500].

[42] M. Rodekamp et al., *Second Moments of Nucleon Unpolarized, Polarized, and Transversity Parton Distribution Functions from Lattice QCD at the Physical Point*, 2401.05360.

[43] C. Alexandrou et al., *Moments of nucleon generalized parton distributions from lattice QCD simulations at physical pion mass*, *Phys. Rev. D* **101** (2020) 034519 [1908.10706].

[44] C. Alexandrou et al., *Complete flavor decomposition of the spin and momentum fraction of the proton using lattice QCD simulations at physical pion mass*, *Phys. Rev. D* **101** (2020) 094513 [2003.08486].

[45] S. Mondal et al., *Moments of nucleon isovector structure functions in* $2 + 1 + 1$*-flavor QCD*, *Phys. Rev. D* **102** (2020) 054512 [2005.13779].

[46] S. Mondal et al., *Nucleon isovector momentum fraction, helicity and transversity moment using Lattice QCD*, *PoS* **LATTICE2021** (2021) 513 [2201.00067].

[47] L. A. Harland-Lang et al., *Parton distributions in the LHC era: MMHT 2014 PDFs*, *Eur. Phys. J. C* **75** (2015) 204 [1412.3989].

[48] S. Dulat et al., *New parton distribution functions from a global analysis of quantum chromodynamics*, *Phys. Rev. D* **93** (2016) 033006 [1506.07443].

[49] H1, ZEUS collaboration, *Combination of measurements of inclusive deep inelastic $e^{\pm}p$ scattering cross sections and QCD analysis of HERA data*, *Eur. Phys. J. C* **75** (2015) 580 [1506.06042].

[50] A. Accardi et al., *Constraints on large-x parton distributions from new weak boson production and deep-inelastic scattering data*, *Phys. Rev. D* **93** (2016) 114017 [1602.03154].

[51] S. Alekhin et al., *Parton distribution functions, α_s, and heavy-quark masses for LHC Run II*, *Phys. Rev. D* **96** (2017) 014011 [1701.05838].

[52] NNPDF collaboration, *Parton distributions from high-precision collider data*, *Eur. Phys. J. C* **77** (2017) 663 [1706.00428].

[53] T.-J. Hou et al., *New CTEQ global analysis of quantum chromodynamics with high-precision data from the LHC*, *Phys. Rev. D* **103** (2021) 014013 [1912.10053].

[54] D. de Florian et al., *Extraction of Spin-Dependent Parton Densities and Their Uncertainties*, *Phys. Rev. D* **80** (2009) 034030 [0904.3821].

[55] N. Salone et al., *Study of CP violation in hyperon decays at super-charm-tau factories with a polarized electron beam*, *Phys. Rev. D* **105** (2022) 116022 [2203.03035].

[56] P. L. J. Petrak et al., *Sigma terms of the baryon octet in $N_f = 2 + 1$ QCD with Wilson quarks*, *Proc. Sci.* **LATTICE2022** (2023) 112 [2301.03871].

[57] Jülich Supercomputing Centre, *JUWELS: Modular Tier-0/1 Supercomputer at the Jülich Supercomputing Centre*, *J. of Large-Scale Research Facilities* **5** (2019) A135.

[58] Jülich Supercomputing Centre, *JURECA: Modular supercomputer at Jülich Supercomputing Centre*, *J. of Large-Scale Research Facilities* **4** (2018) A132.
[59] Jülich Supercomputing Centre, *HDF Cloud – Helmholtz Data Federation Cloud Resources at the Jülich Supercomputing Centre*, *J. of Large-Scale Research Facilities* **5** (2019) A137.
[60] M. Lüscher et al., *Lattice QCD with open boundary conditions and twisted-mass reweighting*, *Comput. Phys. Commun.* **184** (2013) 519 [1206.2809].
[61] Y. Nakamura et al., *BQCD - Berlin quantum chromodynamics program*, *Proc. Sci.* **LATTICE2010** (2010) 040 [1011.0199].
[62] SciDAC, LHP and UKQCDs collaboration, *The Chroma software system for lattice QCD*, *Nucl. Phys. B Proc. Suppl.* **140** (2005) 832 [hep-lat/0409003].
[63] S. Heybrock et al., *Adaptive algebraic multigrid on SIMD architectures*, *Proc. Sci.* **LATTICE2015** (2016) 036 [1512.04506].
[64] P. Georg et al., *DD-αAMG on QPACE 3*, *EPJ Web Conf.* **175** (2018) 02007 [1710.07041].
[65] A. Frommer et al., *Adaptive aggregation based domain decomposition multigrid for the lattice Wilson Dirac operator*, *SIAM J. Sci. Comput.* **36** (2014) A1581 [1303.1377].
[66] M. Lüscher, *Deflation acceleration of lattice QCD simulations*, *J. High Energy Phys.* **12** (2007) 011 [0710.5417].
[67] J. D. Hunter, *Matplotlib: A 2d graphics environment*, *Comput. Sci. Eng.* **9** (2007) 90.